

“Super-resolution” holographic optical tweezers array

Keisuke Nishimura,* Hiroto Sakai, and Taro Ando†
Central Research Laboratory, Hamamatsu Photonics K.K.,
Hirakuchi, Hamana-Ku, Hamamatsu-City, 434-8601, Japan

Takafumi Tomita and Sylvain de Léséleuc
Institute for Molecular Science, National Institutes of Natural Sciences, Myoudaiji, Okazaki, 444-0867, Japan

Aligning light spots into arbitrary shapes is a fundamental challenge in holography, leading to various applications across diverse fields in science and engineering. However, as the spot interval approaches the wavelength of light, interference effects among the spots become prominent, which complicates the generation of a distortion-free alignment. Herein, we introduce a hologram design method based on the optimisation of a nonlinear cost function using a holographic phase pattern as the optimisation parameter. We confirmed a spot interval of $0.952(1) \mu\text{m}$ in a 5×5 multispot pattern on the focal plane of a high-numerical-aperture (0.75) objective by observing the near-infrared (wavelength: 820 nm) holographic output light from a spatial light modulator device, a result which overcomes the limitation of a few micrometres under similar conditions. Furthermore, the definition of the Rayleigh diffraction limit is refined by considering the separation of spots and the spot interval, thereby concluding the achievement of “super-resolution.” The proposed method is expected to advance laser fabrication, scanning laser microscopy, and cold atom physics, among other fields.

INTRODUCTION

Holography, which involves the control and utilisation of both the amplitude and phase of light, has provided numerous benefits—ranging from academic to practical applications—to the modern society for more than seventy years [1, 2]. The technological advancement of optical devices has accelerated the progress of holography; notably, the spatial light modulator (SLM) allows for the direct control of light wavefronts through the optical properties of liquid-crystal molecules [3]. Furthermore, the concept of a computer-generated hologram (CGH) facilitates the on-demand generation of desired light patterns by computing a phase pattern that reproduces the required output [4]. Holographic methods that modulate the light phase using SLMs are widely applied because of their high light utilisation efficiency [5, 6].

Generating light spot arrays is another application of holography, with uses in laser fabrication [7, 8], scanning laser microscopy [9], and cold atom physics. Holographic optical tweezers are vital tools for aligning atoms in an array of arbitrary shapes [10–14], where the quality and spacing of the spot arrays affect the reproducibility of the atom alignment and the strength of interactions between atoms. Generating short-spaced array patterns without distortions is a technical challenge; however, this endeavour addresses a general and fundamental issue in optics, namely, the realisation of super-resolution [15–18].

A common indicator used to determine whether adjacent light spots can be visually distinguished in microscopy is Rayleigh’s criterion [19]. This criterion states

that two spots cannot be distinguished if their spacing is less than the distance from the centre to the first minimum of the “Airy disk,” which is the diffraction pattern of a circular aperture under uniform illumination. However, Rayleigh’s criterion is, at most, semiquantitative and applies only to the observation of incoherent point sources. In fact, under Rayleigh’s criterion, the two Airy disks appear almost merged, which raises the question of whether each spot functions appropriately as an independent optical tweezer. This directs us to reconsider or modify the criteria according to the context of the application.

In this study, we propose a computer-generated hologram (CGH) design method that effectively generates a well-separated fine multispot light array. The proposed method is based on the optimisation of a nonlinear cost function, with the holographic phase pattern serving as the optimisation parameter. The cost function is defined as the correlation between a given target pattern and the output light pattern, which results from the light propagation from the phase distribution in the CGH. Additionally, we establish a quantitative super-resolution criterion for a multispot light array, based on the interrelationship between two conditions: spot spacing and separation of spots. The spot array is considered to achieve super-resolution if either the observed spot separation or the spacing is superior to that of two adjacent Airy disks aligned to satisfy the other conditions. By reproducing CGHs for a 5×5 multispot pattern with near-infrared light ($\lambda = 820 \text{ nm}$), a spot spacing of $0.952(1) \mu\text{m}$ was confirmed for the focal plane of a high-numerical-aperture ($\text{NA} = 0.75$) objective, which overcomes the limitation to a few micrometres under similar conditions.

* keisuke.nishimura@hpk.co.jp

† taro@crl.hpk.co.jp

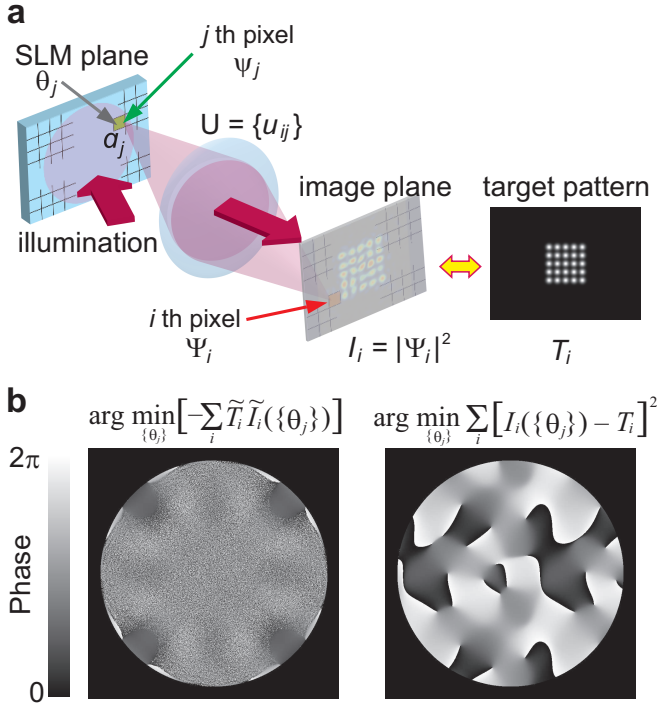


FIG. 1. **Hologram design concept.** **a**, Schematic of CGH design procedure. On the SLM plane, user-defined phase θ_j is attached to incident light amplitude a_j to make output light amplitude of SLM to be $\psi_j = a_j e^{i\theta_j}$. Light propagation, expressed symbolically by an illustration of a lens, acts as a unitary transformation on ψ_j to yield light amplitude on the image plane, Ψ_i . Comparison of output pattern, $I_i = |\Psi_i|^2$, and target pattern, T_i , provides a guide to update θ_j . **b**, Holographic phase patterns for the 5×5 square lattice pattern optimised by CGM using FOI (left) and RSS (right) cost function.

HOLOGRAM DESIGN FOR FINE SPOT ARRAYS

Figure 1a illustrates the concept of CGH design using a reflection-type SLM. For simplicity, the two-dimensional position on the SLM plane is denoted by j , which can be regarded as a vector index. The SLM applies a phase shift θ_j to the incident light amplitude a_j at the j th position. Consequently, the output light amplitude from the SLM is expressed as $\psi_j = a_j \exp(i\theta_j)$.

The position in the image plane can be specified by introducing another vector i to approximately represent the light propagating from the SLM to the image plane using the Fourier transform matrix $U = \{u_{ij}\}$. Therefore, the light amplitude on the image plane Ψ_i is related to ψ_j as follows:

$$\Psi_i = \sum_j u_{ij} \psi_j, \quad (1)$$

and the output pattern is $I_i = |\Psi_i|^2$. The CGH design is a problem of determining $\{\theta_j\}$ for the desired target pat-

tern T_i under fixed illumination conditions corresponding to $\{a_j\}$.

There are two methods for CGH design, which involve calculating the phase distribution $\{\theta_j\}$ to obtain the desired output patterns: self-consistent iterations and optimisation-based methods. A well-known example of the former is the iterative Fourier transform algorithm (IFTA) [6], which determines $\{\theta_j\}$ self-consistently by repeatedly performing light propagation calculations while imposing constraints on the light amplitudes on the SLM and image planes (Fig. 1a). In contrast, optimisation-based methods determine the optimal CGH according to the degree of correspondence between $I_i(\{\theta_j\})$ and T_i . Although optimisation-based methods require more computational resources, they offer higher computational stability and flexibility in designing CGHs.

The optimisation-based CGH design method utilising the analytical gradient of the cost function was first proposed by Harte [20]. In this approach, the set $\{\theta_j\}$ is determined by optimising the following cost function:

$$f_{\text{RSS}}(\{\theta_j\}) = \sum_i [I_i(\{\theta_j\}) - T_i]^2, \quad (2)$$

which involves minimising the residual sum of squares (RSS) between I_i and T_i . Note that I_i and T_i are normalised such that their sums equal unity, and I_i is an explicit function of the phase distribution. This method provides holographic phase patterns similar to those obtained by IFTA. However, unique functionalities can be introduced into CGH design by selecting different cost functions [21]. In this study, we propose using the ‘‘fidelity of intensity’’ (FOI) as the cost function:

$$f_{\text{FOI}}(\{\theta_j\}) = - \sum_i \tilde{I}_i(\{\theta_j\}) \tilde{T}_i, \quad (3)$$

where $\tilde{\cdot}$ denotes a quantity normalised with respect to its Euclidean norm.

Gradient-based optimisation methods including the conjugate gradient method (CGM) require computing the gradients of the cost function, which often becomes challenging for more complex functions than those considered in this study. Fortunately, $\partial f_{\text{FOI}} / \partial \theta_j$ can be explicitly expressed as follows:

$$\frac{\partial f_{\text{FOI}}}{\partial \theta_j} = \frac{2}{\mathcal{N}_I} \sum_i (-\tilde{T}_i + f_{\text{FOI}} \tilde{I}_i) \text{Im}[u_{ij}^* \Psi_j \psi_i^*], \quad (4)$$

where $\mathcal{N}_I (\equiv \sqrt{\sum_i I_i^2})$ represents the Euclidean norm of $\{I_i\}$. This expression enables efficient coding that completes large-scale optimisation in a reasonable time, typically 10–20 min, starting with an arbitrary random pattern. Figure 1b illustrates the examples of designed CGHs obtained using the FOI and RSS methods, respectively. Despite the scepticism regarding the practical effectiveness of the FOI-designed CGH (Fig. 1b left), we assure that *it generally performs well*. See Methods for details (of the hologram design).

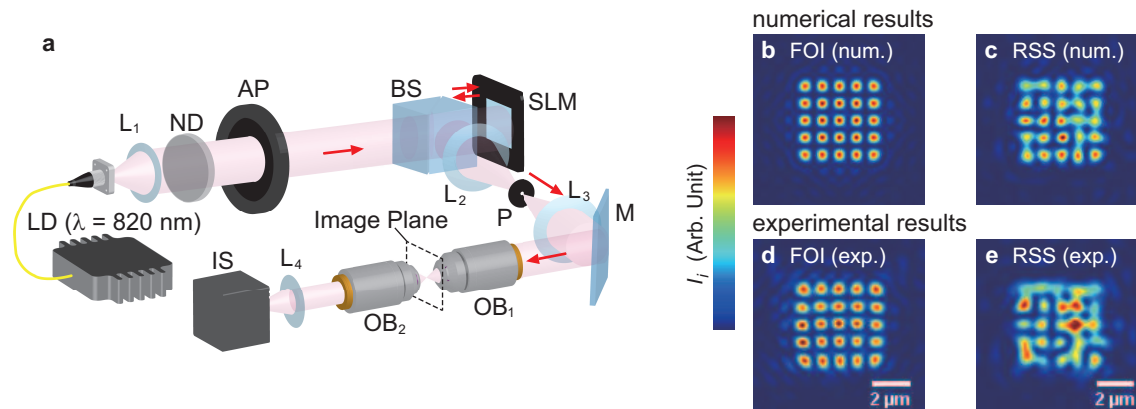


FIG. 2. **Hologram reproduction experiments and results.** **a.** Schematic of experimental setup for hologram reproduction. Output from fibre-coupled laser diode (LD) is collimated by an achromatic lens (L_1) and is projected through a neutral density filter (ND) and an aperture (AP) on the active area of a spatial light modulator device (SLM), on which phase distribution of a displayed holographic phase pattern is attached. A $4f$ -telescope system comprising a pair of achromatic lenses (L_2 and L_3) is utilised to project the SLM plane onto the entrance pupil of an objective lens (OB_1). The reproduced images are captured on the focal plane of OB_1 , referred to as the “image plane,” using a CMOS image sensor (IS) through another objective lens of identical specifications (OB_2) and an achromatic lens (L_4) functioning as a tube lens. A pinhole (P) is placed at the focus of the $4f$ system to eliminate the zeroth-order and stray components. The numerical and observed images reproduced from FOI- and RSS-designed CGHs are presented as well. **b, c:** numerical results for **b** FOI- and **c** RSS-designed CGHs. **d, e:** experimental results of **d** FOI- and **e** RSS-designed CGHs. The spot spacing is set to 1.8 pixels in a common target pattern, corresponding to $0.952(1) \mu\text{m}$ on the image plane. All results were obtained without any adaptive modifications to the hologram patterns.

RESULTS

Hologram reproduction and analyses. To investigate the properties of the proposed method, the reproduced images of RSS- and FOI-designed CGHs were compared for target patterns as 5×5 square spot arrays with varying spot spacing. The reproduced images of CGHs were observed using the experimental setup illustrated in Fig. 2a. Figures 2b-2e display examples of numerical and experimental images reproduced from FOI- and RSS-designed CGHs for a target spot spacing of 1.8 pixels, which corresponds to $0.9225 \mu\text{m}$ in the experimental setup (refer to Methods).

When the spot spacing of the target pattern is less than two pixels, the spots in the numerically reproduced images begin to merge for the RSS-designed CGHs, whereas the results of FOI-designed ones maintain clear separation. However, in the experimental reproduction, even the images from FOI-designed CGHs cannot maintain spot separation for target spot spacing of less than 1.8 pixels.

Although adaptive adjustment of hologram patterns is frequently incorporated into CGH designs to enhance the image quality of holographic outputs [22, 23], the current results were obtained without any post-modification. In our experiments, a 5×5 square spot array was selected as the target pattern to minimise the computational load, which increases with the number of spots, and to verify the principles of the proposed method.

The mean spot spacing is $0.952(1) \mu\text{m}$ for Fig. 2d, which cannot be attained by any other existing holo-

gram design methods under similar optical conditions. Actually, reproduced patterns on the focal plane was observed by super-resolution optical pattern measurement [24, 25] with the consequence that the spot spacing was estimated as less than $1 \mu\text{m}$ using 852 nm trapping beam with a high-NA objective (NA=0.75 in design). Preliminary experiments on fluorescence image observation also confirmed trapping of atoms on the focal plane. These results will be reported elsewhere in the future.

Spot uniformity and light utilisation efficiency.

Considering the scope of this study, the evaluation of the reproduced images should be based on the characteristic properties of light-spot arrays. One might assume that the FOI itself serves as a measure of the quality of the reproduced images. However, FOI primarily reflects the total correspondence between the output and target patterns. Therefore, we investigated the properties of the reproduced images in terms of the uniformity of the light spot array and light utilisation efficiency.

The spot uniformity and utilisation efficiency of the images reproduced using FOI- and RSS-designed CGHs are presented in Table I. The results reveal that the FOI method exhibits small variations in spot power but demonstrates low light utilisation efficiency, despite employing phase-only modulation. In contrast, the RSS results display the opposite behaviour. Uniformity was suppressed in both numerical and experimental results, whereas the numerical and experimental values of light utilisation efficiency were similar. Thus, the FOI method can generate high-quality spot arrays in terms of uniformity and stability, although at the expense of efficiency.

TABLE I. **Properties of reproduced spot arrays.** The spatial uniformity is assessed by the relative standard deviation (SD), which is the ratio of the SD to the mean value, in the powers of the 5×5 light spots that form the spot array. The power of each light spot is estimated by applying fitting analysis to an output image (Methods). The light utilisation efficiency is calculated as the ratio of the output light power (measured by a power meter through a 1-mm-diameter pinhole placed on the image plane) to the illumination power measured on the SLM plane. The light utilisation efficiency is simply stated as the sum of I_i over the area displayed in Fig. 2 for numerically reproduced images. The value and error of a physical quantity indicate the mean value and standard error (SE), respectively, in a series of quantities evaluated numerically or experimentally from 20 CGHs, each designed by starting from a different initial random pattern to generate a common target.

	Spot uniformity		Utilisation efficiency	
	FOI	RSS	FOI	RSS
Numerical	$1.21(4) \times 10^{-2}$	$5.6(10) \times 10^{-2}$	0.120(3)	0.928(4)
Experimental	$9.70(15) \times 10^{-2}$	$2.7(3) \times 10^{-1}$	0.127(2)	0.64(3)

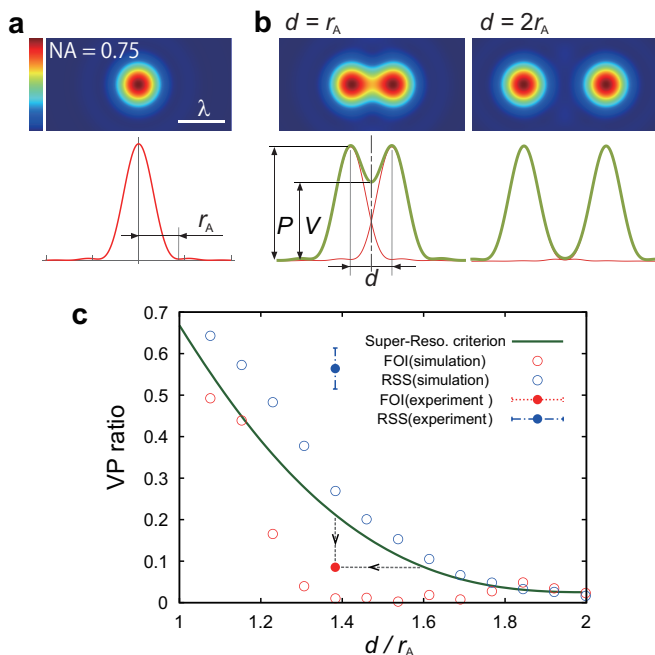


FIG. 3. **Spacing and separation of adjacent light spots.**

a, Focal pattern (top) and profile (bottom) of Airy disk [NA = 0.75(air)]. Red line in the bottom plot shows cross-sectional profile corresponding to the focal pattern, where r_A refers to the Airy-disk radius. **b**, Focal patterns and profiles of incoherent sums of two Airy disks aligned at distances of $d = r_A$ (left) and $2r_A$ (right). In the bottom plots, thick green lines display the profiles of the incoherent sums, whereas thin red lines indicate those of individual Airy disks. Definitions of peak (P) and valley (V) are illustrated as well. **c**, (Solid green line) The relationship between the VP ratio and spot spacing for incoherent sums of adjacent Airy disks is depicted, where the traditional Rayleigh diffraction limit corresponds to $VP = 0.66$ at $d/r_A = 1$. Open circles represent VP ratios for numerically reproduced images from FOI- (red open circles) and RSS-designed (blue open circles) CGHs, while closed circles represent those for the corresponding observed patterns, i.e., Figs. 2c (red closed circle) and d (blue closed circle), respectively. Error bars (SEs) are determined similarly to those in Table I but are smaller than the size of the plot symbols, except for the experimental result of an RSS-designed CGH.

Relation between spacing and separation of spot array.

FOI-designed holograms can generate high-quality spot arrays with extremely narrow spacing. To evaluate the behaviour of spot arrays within the diffraction-limit regions, the focal patterns calculated under a high-NA [= 0.75 (air)] condition are displayed in Fig. 3. Note that all numerical results in Fig. 3 were calculated using vector Debye formulas [26–30], as the focal patterns of coherent light are affected by the vector nature of the light amplitude under NA conditions greater than 0.70. The Airy disk pattern calculated assuming circularly polarised light is illustrated in Figure 3a.

The Rayleigh-limit conditions portrayed on the left in Fig. 3b present the adjacent light spots (Airy disks) as inadequately separated, while well-separated light spots, as displayed on the right of Fig. 3b, are desirable for maintaining a high aspect ratio in applications such as laser processing and suppression of background noise in scanning laser microscopy. Therefore, a factor other than

spot spacing is required for a proper evaluation of spot-array patterns while considering their applications.

The valley-to-peak (VP) ratio of a spot array along with the inverse of the peak-to-valley ratio was introduced as a metric for spot separation. A smaller VP ratio indicates a clear separation of adjacent light spots. The VP ratio is advantageous because of its availability and robustness in derivation under unfavourable conditions compared to other metrics, such as the size of each light spot. To derive the VP ratio of the reproduced spot-array image, the peak positions were determined by fitting the reproduced images (Methods). The peak value refers to the mean of I_i at the peak positions of all the bright spots, whereas the valley value refers to the mean of I_i at all the midpoints between the adjacent peaks. Thus, the VP ratio was evaluated as the ratio of the valley value to the peak value.

The blue (red) open circles displayed in Fig. 3c represent the VP ratios of numerically reproduced images from hologram patterns designed by the FOI (RSS) cost

method, whereas the blue (red) closed circles indicate those derived from the experimental images. In terms of the VP ratio, the proposed FOI method outperforms the conventional RSS method in the range of ($1 < d/r_A < 2$).

DISCUSSIONS

The super-resolution criterion can be defined as both definite and quantitative. In considering the relationship between physical quantities involving spot separation, the traditional Rayleigh diffraction limit is established for an incoherent superposition of two Airy disks. Thus, this approach should be logically followed. We propose to determine whether a spot array exhibits “super-resolution” by examining the relationship between the spacing d and the VP ratio of two incoherent Airy disks, as illustrated by the solid green line in Fig. 3(c). This criterion quantitatively delineates a limit that cannot be surpassed using incoherent light and is beneficial for discussing the separability of multispot patterns using coherent light.

The area below the green line can be regarded as a super-resolution region, where the separation of adjacent spots is superior to the criterion for fixed spot spacing, or where the spot spacing is smaller than the criterion for a fixed VP ratio. According to the extended super-resolution criterion, the numerical VP values in Fig. 3(c) suggest the potential of FOI-designed holograms to generate super-resolution light spot arrays in the regime $d/r_A < 1.8$. In particular, superior spot separation is anticipated for $1.3 < d/r_A < 1.7$. The RSS-designed holograms generate holograms surrounding the criterion but cannot overcome these limitations. The experimental VP ratios at $d/r_A = 1.4$ in Fig. 3(c) exhibit moderately larger values than the numerical ones, suggesting the influence of extrinsic factors in the experiments, such as residual optical aberrations. Nevertheless, we emphasise that the results of the FOI-cost method still fall within the super-resolution regime. Refer to Supplementary Information for further details.

As described in Methods, instabilities exist in the hologram design and optical reproduction, which can be distinguished by comparing the numerical and experimental results. A point of issue in this comparison is that errors in the numerical light utilisation efficiencies were similar for both the FOI and RSS methods, as listed in Table I. Interestingly, the accuracy of the CGM procedure was the dominant contributor to these errors, which was the only common factor between the FOI and RSS methods. The CGM procedure contributes toward achieving higher numerical stability compared to self-consistent iterations like the IFTA method.

In contrast, the numerical and experimental values of light utilisation efficiency are similar for the FOI method, implying that the FOI method is tolerant to experimental disturbances concerning light utilisation efficiency, which is a global property of light spot arrays. However, this argument does not apply to spot uniformity, which ex-

plains the local properties of the spot arrays. The numerical results, including both the values and errors of spot uniformity, reveal distinct differences between the FOI and RSS methods, as outlined in Table I. Thus, spot uniformity is affected by the selection of the cost function.

However, this difference reduced marginally in the experimental results, implying a nonnegligible contribution from experimental factors such as aberrations in optical trains. The FOI method generates super-resolution spot arrays of higher quality than the RSS method, and the structural stability of the FOI method is maintained to a certain extent even in the presence of experimental disturbances.

The subsequent question is: *how does the FOI method generate super-resolution spot arrays?* A well-known example is the phase shift method [31] used in lithography. Although lithography differs from holography in terms of near and far-field light propagation phenomena, this technology has attempted to overcome the diffraction limits by controlling the phase distribution of coherent light. The RSS method can be classified under this type of approach owing to its high light utilisation efficiency and globally smooth CGHs, as illustrated in Fig. 1b.

In contrast, the FOI-designed CGH shown in Fig. 1b presents a phase profile with prominent high-frequency components that cause diffusive light propagation. This leads to the characteristics of the FOI method, namely, low light utilisation efficiency. Therefore, FOI-designed CGHs may function as complex amplitude modulation phase holograms [32–35] to remove the undesired light components that prevent super-resolution and cause interference, which induces instability in the holographically reproduced images. Conversely, the current results indicate a limitation of phase-only modulation approaches and the necessity of removing undesired light components to achieve super-resolution spot arrays.

Before concluding the paper, we discuss the numerical properties of the FOI cost function. In CGH design problems, an “absolute” solution satisfying $I_i = T_i$ is not possible within a set of physical solutions at all instances due to the nature of light propagation. Consequently, CGHs designed using optimisation-based methods generally rely on cost functions. Here, it is essential to focus on the behaviour of the cost function rather than its superficial form. In fact, we can readily confirm that $\sum (\tilde{I}_i - \tilde{T}_i)^2 = 2 - 2 \sum \tilde{I}_i \tilde{T}_i$ holds, indicating the equivalence of the FOI and RSS cost functions under Euclidean normalisation. Thus, one can infer that Euclidean normalisation itself plays a crucial role in generating CGHs for super-resolution spot array patterns. Although we were unable to establish a mathematically rigorous description of the significant changes in the reproduced images due to the cost functions, it is still worthwhile to discuss this briefly.

Consider a test target pattern such that $T_i = c > 0$ only at separated M points, among N lattice points in the image plane ($M \leq N$). The support for T_i is denoted

by α as follows: $\alpha = \{\forall i | T_i \neq 0\}$. The target pattern satisfies $T_i = 1/M$ ($i \in \alpha$) for the total-sum normalisation, whereas $\tilde{T}_i = 1/\sqrt{M}$ ($i \in \alpha$) holds for Euclidean normalisation. Therefore, the FOI cost function becomes $f_{\text{FOI}} = -(1/\sqrt{M}) \sum_{i \in \alpha} \tilde{T}_i$. However, the RSS cost provides:

$$\begin{aligned} \sum_i (I_i - T_i)^2 &= 2 - \sum'_{i \neq k} T_i T_k - 2 \sum_{i \in \alpha} I_i T_i - \sum'_{i \neq k} I_i I_k \\ &= \left(1 + \frac{1}{M}\right) - \frac{2}{M} \sum_{i \in \alpha} I_i - \sum'_{i \neq k} I_i I_k, \quad (5) \end{aligned}$$

where $\sum I_i^2 = 1 - \sum'_{i \neq k} I_i I_k$ and a similar relation for T_i was used for the aforementioned deformations. Note that the sum of the output values over α commonly works to reduce both FOI and RSS cost values, despite the difference in normalisation. However, an additional factor in f_{RSS} reduces the cost value: the last term of Equation (5). This term accounts for the autocorrelation of the output pattern independent of the target, and it broad-

ens the light spots, which is favourable for reducing f_{RSS} .

CONCLUSIONS

This study discovered that the quality of narrow holographic optical lattice patterns could be significantly improved by utilising the FOI-cost method for hologram optimisation, as opposed to the traditional RSS-cost method. We have developed a super-resolution criterion specifically for arrays of light spots, which is based on the spacing of the spots and the VP ratio of the incoherently superimposed Airy disks. The multipot patterns generated in the present experiments satisfied this criterion, representing a key advancement for subsequent cold atom experiments employing holographic techniques [25]. The potential applications of this method are not limited to cold atoms; it also holds promise for laser processing [7, 8] and bioimaging [9]. In future, we intend to establish a comprehensive understanding of the relationship between other hologram design methods, such as IFTA and its derivatives, and optimisation-based methods. This exploration is expected to evolve, thereby expanding the potential application areas of the proposed method.

-
- [1] D. Gabor, A new microscopic principle, *Nature* **161**, 777 (1948).
 - [2] D. Gabor and W. L. Bragg, Microscopy by reconstructed wave-fronts, *Proceedings of the Royal Society of London. Series A. Mathematical and Physical Sciences* **197**, 454 (1949).
 - [3] G. Lazarev, P.-J. Chen, J. Strauss, N. Fontaine, and A. Forbes, Beyond the display: phase-only liquid crystal on silicon devices and their applications in photonics, *Opt. Express* **27**, 16206 (2019).
 - [4] D. Pi, J. Liu, and Y. Wang, Review of computer-generated hologram algorithms for color dynamic holographic three-dimensional display, *Light: Science & Applications* **11**, 10.1038/s41377-022-00916-3 (2022).
 - [5] L. B. Lesem, P. M. Hirsch, and J. A. Jordan, The kinoform: A new wavefront reconstruction device, *IBM Journal of Research and Development* **13**, 150 (1969).
 - [6] F. Wyrowski and O. Bryngdahl, Iterative fourier-transform algorithm applied to computer holography, *J. Opt. Soc. Am. A* **5**, 1058 (1988).
 - [7] M. Sakakura, T. Sawano, Y. Shimotsuma, K. Miura, and K. Hirao, Fabrication of three-dimensional 1×4 splitter waveguides inside a glass substrate with spatially phase modulated laser beam, *Optics express* **18**, 12136 (2010).
 - [8] M. Sakakura, T. Sawano, Y. Shimotsuma, K. Miura, and K. Hirao, Improved phase hologram design for generating symmetric light spots and its application for laser writing of waveguides, *Opt. Lett.* **36**, 1065 (2011).
 - [9] V. Nikolenko, B. O. Watson, R. Araya, A. Woodruff, D. S. Peterka, and R. Yuste, Slm microscopy: scanless two-photon imaging and photostimulation using spatial light modulators, *Frontiers in neural circuits* **2**, 5 (2008).
 - [10] F. Nogrette, H. Labuhn, S. Ravets, D. Barredo, L. Béguin, A. Vernier, T. Lahaye, and A. Browaeys, Single-atom trapping in holographic 2d arrays of microtraps with arbitrary geometries, *Physical Review X* **4**, 021034 (2014).
 - [11] H. Labuhn, D. Barredo, S. Ravets, S. de Léséleuc, T. Macrì, T. Lahaye, and A. Browaeys, Tunable two-dimensional arrays of single rydberg atoms for realizing quantum ising models, *Nature* **534**, 667 (2016).
 - [12] S. Ebadi, T. T. Wang, H. Levine, A. Keesling, G. Semeghini, A. Omran, D. Bluvstein, R. Samajdar, H. Pichler, W. W. Ho, S. Choi, S. Sachdev, M. Greiner, V. Vuletić, and M. D. Lukin, Quantum phases of matter on a 256-atom programmable quantum simulator, *Nature* **595**, 227 (2021).
 - [13] D. Bluvstein, H. Levine, G. Semeghini, T. T. Wang, S. Ebadi, M. Kalinowski, A. Keesling, N. Maskara, H. Pichler, M. Greiner, V. Vuletić, and M. D. Lukin, A quantum processor based on coherent transport of entangled atom arrays, *Nature* **604**, 451 (2022).
 - [14] Y. Chew, T. Tomita, T. P. Mahesh, S. Sugawa, S. de Léséleuc, and K. Ohmori, Ultrafast energy exchange between two single rydberg atoms on a nanosecond timescale, *Nature Photonics* **16**, 724 (2022).
 - [15] E. Betzig, G. H. Patterson, R. Sougrat, O. W. Lindwasser, S. Olenych, J. S. Bonifacino, M. W. Davidson, J. Lippincott-Schwartz, and H. F. Hess, Imaging intracellular fluorescent proteins at nanometer resolution, *Science* **313**, 1642 (2006).
 - [16] S. T. Hess, T. P. Girirajan, and M. D. Mason, Ultra-high resolution imaging by fluorescence photoactivation localization microscopy, *Biophysical Journal* **91**, 4258 (2006).

- [17] M. J. Rust, M. Bates, and X. Zhuang, Sub-diffraction-limit imaging by stochastic optical reconstruction microscopy (STORM), *Nature Methods* **3**, 793 (2006).
- [18] M. Heilemann, S. van de Linde, M. Schüttelz, R. Kasper, B. Seefeldt, A. Mukherjee, P. Tinnefeld, and M. Sauer, Subdiffraction-resolution fluorescence imaging with conventional fluorescent probes, *Angewandte Chemie International Edition* **47**, 6172 (2008).
- [19] L. Rayleigh, Xxi. investigations in optics, with special reference to the spectroscope, *Phyl. Mag., S. 5.* **8**, 10.1080/14786447908639684 (1879).
- [20] T. Harte, G. D. Bruce, J. Keeling, and D. Cassettari, Conjugate gradient minimisation approach to generating holographic traps for ultracold atoms, *Optics Express* **22**, 26548 (2014).
- [21] D. Bowman, T. L. Harte, V. Chardonnet, C. De Groot, S. J. Denny, G. Le Goc, M. Anderson, P. Ireland, D. Cassettari, and G. D. Bruce, High-fidelity phase and amplitude control of phase-only computer generated holograms using conjugate gradient minimisation, *Optics express* **25**, 11692 (2017).
- [22] N. Matsumoto, T. Inoue, T. Ando, Y. Takiguchi, Y. Ohtake, and H. Toyoda, High-quality generation of a multispot pattern using a spatial light modulator with adaptive feedback, *Opt. Lett.* **37**, 3135 (2012).
- [23] S. P. Poland, N. Krstajić, R. D. Knight, R. K. Henderson, and S. M. Ameer-Beg, Development of a doubly weighted gerchberg–saxton algorithm for use in multibeam imaging applications, *Opt. Lett.* **39**, 2431 (2014).
- [24] T. Tomita, R. Villela, Y. Chew, T. P. Mahesh, H. Sakai, K. Nishimura, T. Ando, S. De Léséleuc, and K. Ohmori, Atom camera: Super-resolution imaging of an optical field with a single ultracold atom in an optical tweezers (The 27th International Conference on Atomic Physics (ICAP2022), Toronto).
- [25] T. Tomita, Y. Chew, R. Villela, T. P. Mahesh, H. Sakai, K. Nishimura, T. Ando, S. De Léséleuc, and K. Ohmori, Atom camera: Super-resolution scanning microscope of a light pattern with a single ultracold atom, In preparation. ().
- [26] B. Richards and E. Wolf, Electromagnetic diffraction in optical systems II. Structures of the image field in an aplanatic system, *Proc. Roy. Soc. (London) A* **253**, 358 (1959).
- [27] A. Boivin and E. Wolf, Electromagnetic field in the neighborhood of the focus of a coherent beam, *Phys. Rev.* **138**, B1561 (1965).
- [28] K. S. Youngworth and T. G. Brown, Focusing of high numerical aperture cylindrical-vector beams, *Opt. Express* **7**, 77 (2000).
- [29] Y. Zhao, J. S. Edgar, G. D. M. Jeffries, D. McGloin, and D. T. Chiu, Spin-to-orbital angular momentum conversion in a strongly focused optical beam, *Phys. Rev. Lett.* **99**, 073901 (2007).
- [30] P. B. Monteiro, P. A. M. Neto, and H. M. Nussenzweig, Angular momentum of focused beams: Beyond the paraxial approximation, *Phys. Rev. A* **79**, 033830 (2009).
- [31] M. D. Levenson, N. Viswanathan, and R. A. Simpson, Improving resolution in photolithography with a phase-shifting mask, *IEEE Transactions on electron devices* **29**, 1828 (1982).
- [32] J. P. Kirk and A. L. Jones, Phase-only complex-valued spatial filter*, *J. Opt. Soc. Am.* **61**, 1023 (1971).
- [33] J. A. Davis, D. M. Cottrell, J. Campos, M. J. Yzuel, and I. Moreno, Encoding amplitude information onto phase-only filters, *Appl. Opt.* **38**, 5004 (1999).
- [34] V. Arrizón, U. Ruiz, R. Carrada, and L. A. González, Pixelated phase computer holograms for the accurate encoding of scalar complex fields, *J. Opt. Soc. Am. A* **24**, 3500 (2007).
- [35] T. Ando, Y. Ohtake, N. Matsumoto, T. Inoue, and N. Fukuchi, Mode purities of laguerre–gaussian beams generated via complex-amplitudemodulation using phase-only spatial light modulators, *Opt. Lett.* **34**, 34 (2009).
- [36] H. Kim, M. Kim, W. Lee, and J. Ahn, Gerchberg-saxton algorithm for fast and efficient atom rearrangement in optical tweezer traps, *Optics express* **27**, 2184 (2019).
- [37] S. Inoué, Studies on depolarization of light at microscope lens surfaces: I. The origin of stray light by rotation at the lens surfaces, *Exp. Cell Research* **3**, 199 (1952).
- [38] S. M. Barnett and L. Allen, Orbital angular momentum and nonparaxial light beams, *Opt. Commun.* **110**, 670 (1994).

METHODS

Scale correspondence between hologram and target planes. In a practical CGH design, the SLM plane is typically represented as an $N \times N$ square grid, where N is a positive integer. The active area of the SLM is embedded within this grid by setting $a_j = 0$ outside the active area. The light propagation from the SLM to the image plane can generally be described by a unitary matrix $U = \{u_{ij}\}$, often referred to as the “transfer matrix.” This matrix is approximated by a Fourier transformation when the SLM and image planes are connected using imaging optics. Consequently, the image plane also becomes an $N \times N$ grid because the action of U preserves the grid size.

Suppose hologram reproduction is performed using light of wavelength λ with imaging optics of effective focal length f . In that case, the actual size of the target can be estimated using the relation $\Delta x' = \lambda f / (N \Delta x)$, which describes the relationship between the grid spacings on the SLM and image planes, Δx and $\Delta x'$, respectively.

Details of hologram design. We designed hologram patterns by applying the CGM to minimise the FOI cost function for given target patterns. The number of CGM iterations was set at 1000, which is typically sufficient for the relative decrease in FOI cost per iteration step to be less than 10^{-8} . The minimisation-based hologram design problem does not necessarily yield unique solutions. Therefore, the designed hologram patterns depend on the initial patterns selected, which are prepared by assigning a pseudorandom number (in the range $[0, 2\pi)$) to each lattice point on the grid in the SLM plane.

Note that a sequence of pseudorandom numbers is completely determined by selecting an integer, known as the “random seed.” Different seeds can be selected

to generate various hologram patterns for the same target patterns. The images reproduced from these different hologram patterns can be treated as independent statistical trials to evaluate the statistical errors of the physical quantities obtained through analyses. The error treatments are described in the subsequent section.

Assuming that the hologram and the target planes are connected using Fourier optics, the display hologram patterns are situated in the $800 \text{ px} \times 800 \text{ px}$ region of the phase-only SLM surface. The input and target planes are represented as spatial grids of the same size in the numerical Fourier transform, with the target plane comprising 800×800 points. To increase the effective resolution of the target image by a factor of ten, the method described in [36] was applied to the SLM plane.

Specifically, the hologram region is embedded into the centre of an 8000×8000 grid, where the light amplitude is set to zero outside the hologram. Moreover, we assume that the illumination is a top-hat laser beam, indicating that a_j in Fig. 1a presumes a nonzero constant value within the central circular region of a 360-pixel radius.

Ultimately, the hologram design becomes a 640,000-dimensional numerical optimisation problem. Most computing resources are consumed by repeated evaluations of the cost function and its derivatives, which involve the propagation calculations of the two-dimensional light amplitude distribution expressed by 8000×8000 components. To efficiently perform such large-scale propagation computations, we applied a double-precision complex FFT algorithm running on general-purpose graphics processing units, which achieved a total computational time of less than 30 min.

Numerical optimisation yielded holographic phase patterns as two-dimensional arrays of double-precision floating-point numbers within the interval $[0, 2\pi)$. As the SLM device is designed to handle 8-bit signals, the phase values were discretised into 256-step (8-bit) quantities for practical application. In this text, ‘‘CGHs’’ or ‘‘holographic phase patterns’’ refers to the discretised versions.

Observation of reproduced images. Experiments were conducted using the optical system depicted in Fig. 2. An 820 nm laser diode with a fibre port (LP820-SF80, Thorlabs) served as the light source. The light emitted from the fibres was expanded and collimated using achromatic lenses, which forms a top-hat beam with apertures. The light was directed onto a reflection-type liquid crystal-on-silicon SLM (X13138-01 modified, Hamamatsu) via a beam splitter into lens optics. As displayed in Fig. 1b, phase holograms were displayed on the SLM, which has a pixel pitch of $12.5 \mu\text{m} \times 12.5 \mu\text{m}$. A phase pattern with a constant gradient in a specific axial direction was superimposed to demarcate the non-modulated light components from the reproduced image.

For tight focusing, the hologram plane was transferred through a $4f$ telescope—0.8X-magnification optical system consisting of two achromatic lenses with a focal length of 125 mm and 100 mm—from the entrance pupil

of an objective lens [MRH00401, Nikon: NA = 0.75 (air)]. Focal images were obtained using a 60X-magnification optical system, comprising the same objective lens used for focusing, a achromatic lens with a focal length of 300 mm, and an image sensor (Lumenera, LU135M-IO-WOIR).

If the illuminated area on the SLM plane (i.e., the SLM pixels labelled by $\{\forall j|a_j \neq 0\}$) is not incident on the entrance pupil of the objective lens, it reduces the effective numerical aperture and fails to generate a short spot spacing, thereby limiting the performance of the objective. Therefore, a suitable choice of the illumination area and/or magnification of the transfer optical systems was required.

Data analyses of observed and numerically derived images. The spacing and positions of the spots were determined by fitting the output patterns to the image plane using the following model. This model represents an incoherent superposition of Gaussian spots with a common spot radius, w_0 on uniform background B :

$$I_{\text{fit}} = \sum_k A_k \exp \left[-\frac{(x - x_k)^2 + (y - y_k)^2}{w_0^2/2} \right] + B, \quad (6)$$

where k denotes an index to distinguish the spots, and the peak ‘‘height’’ and position of the k -th spot is expressed as A_k and (x_k, y_k) .

The tilt angle of an image, θ , is included in the practical fitting calculations. Consequently, the fitting model becomes a (three times the number of spots plus three)-dimensional problem, rendering the analysis as computationally demanding. Therefore, the quantitative analyses were restricted to a 5×5 square spot alignment with spacing d . After positioning a peak at (X_0, Y_0) , the other (x_k, y_k) positions are automatically determined as $(X_0 + md, Y_0 + nd)$ for pairs of suitable integers m and n , depending on the geometrical configuration of the target spot array.

Upon determining the positions of the spot peaks, the light power of each spot can be estimated as the sum of the signal levels within a square area (with d on one side), whose centre corresponds to the position of the peak. ‘‘Spot uniformity’’ is then derived as the ratio of the standard deviation to the mean light powers at the twenty-five spots. Regarding the VP ratios, P and V represent the means of the signal levels at the peak and valley positions, respectively, where the valleys were identified as the midpoints of the adjacent peaks.

The number of trials in the analyses of RSS results was reduced because one of the holographic phase patterns obtained using the RSS method was excluded from the experiments and analyses due to the failure of convergence in the hologram design. Although the RSS method successfully yields holographic phase patterns, the reproduced images of the RSS-designed holograms exhibit significant distortions, as depicted in Figures 2c and 2e. In such cases, the aforementioned analysis often fails to

determine the peak positions in the reproduced images. Therefore, we adopted the results of an FOI-designed hologram that was obtained using the same initial random pattern.

Errors in design and reproduction of holograms.

In this study, the error of a physical quantity, defined as SE in a series of quantities, provides a benchmark for the stability of the reproduced images. It includes the effects of the non-uniqueness of the hologram design problem, the convergence criterion set for optimisation in CGH design, the handling of phase values in CGHs (rounded to discrete values), and the numerical/experimental accuracy for hologram reproduction.

The accuracy of the numerical holographic reproduction was equivalent to that of the FFT algorithm and is expected to be negligibly small (less than 5×10^{-5} relative to the root-mean-square error, even for single-precision FFT, as noted in <https://pypi.org/project/pyvkfft/>). This fact justifies neglecting the errors of numerically derived quantities. Therefore, the instabilities in the hologram design and optical reproduction stages, namely, the intrinsic and extrinsic instabilities, can be distinguished by comparing the numerical and experimental results presented in Table I.

DECLARATIONS

Acknowledgements The authors are grateful to H. Toyoda, T. Inoue, and Y. Ohtake of HPK for their encouragement throughout this work, and to T. Watanabe for kind supports on fabrication of optics. We also appreciate discussion and kind support provided by Prof. K. Ohmori of IMS as the leader of ultrafast cold-atom quantum simulator projects. Part of this study was performed under support of JSPS Grant-in-Aid for Specially Promoted Research (grant no. 16H06289). T.T. and S.d.L. also acknowledge partial support by JSPS Grant-in-Aid for Research Activity Start-up (grant nos. 19K23431 and 19K23429, respectively) as well as by MEXT Quantum Leap Flagship Program (MEXT Q-LEAP) JPMXS0118069021 and JST Moonshot R&D Program Grant Number JPMJMS2269.

Author contributions T.A. and K.N. established the basic concept of the study and the hologram-design architecture. H.S. designed and performed the optical experiments as well as contributed to data analyses. K.N. and T.A. performed data analyses and numerical evaluation and wrote the manuscript with contributions from all authors. T.T. and S.d.L. contributed to the discussion from a viewpoint of cold-atom physics based on preliminary experiments.

Data availability Data underlying the results presented in this paper are not publicly available at this time

but may be obtained from the authors upon reasonable request.

Competing interest The authors declare no competing interests.

SUPPLEMENTARY INFORMATION

Vector Debye formula for focal pattern under high-NA conditions. To accurately calculate the diffraction integral, the vector nature of light must be considered to obtain focal patterns that are deemed correct within wave optics [26, 27]. The vector nature of light in the focusing phenomenon is schematically illustrated in Fig. 4. An objective lens modifies the incident light by attaching a spherical wavefront, thereby altering the propagation direction of light towards the centre of the spherical wavefront, known as the geometric focus (Fig. 4a).

As the propagation direction changes, the vector amplitude of the incident light is reduced, inducing a polarisation component in the direction of light propagation (Fig. 4b). This results in an inhomogeneous modulation of the vector light amplitude due to the edge birefringence of the lens (Fig. 4c) [37]. These characteristics are specific to focusing by a high-NA objective lens, and this phenomenon is referred to as depolarisation.

The polarisation vectors of light at the entrance pupil and image space of an objective lens are expressed in Cartesian coordinates, where the z -axis and origin correspond to the optical axis and geometrical focus, respectively (Fig. 4a). Although the coordinates of the entrance pupil and those in the image space are distinct, polarisation vectors can be described in a common Cartesian coordinate system. In general, various coordinate systems are introduced to describe the positions on the entrance pupil and in the image space. The former is expressed in polar coordinates, (r, φ) , whereas the latter uses cylindrical coordinates (ρ, ϕ, z) . The cylindrical and Cartesian coordinates in the image space are compatible through a coordinate transformation.

Note that the azimuth ($= \varphi$) of the entrance pupil represents the directional angle of the spherical wavefront at the pupil exit (Fig. 4a) because an ideal objective lens does not alter the azimuthal direction. The vector Debye formula defines an integral transformation of the vector field of light amplitude from (r, φ) to (ρ, ϕ, z) , as determined by the action of a high-NA objective lens.

In the context of this study, the incident light is assumed to be monochromatic, with a wavelength λ ($= 2\pi/k$). We assumed that the incident light has a spatially homogeneous polarisation and electric field amplitude distribution of the form $e^{-il\varphi} E_{\text{in}}(r)$. The focal patterns of various light beams can be derived from a combination of these distributions.

Thus, the polarisation vector of the incident light is

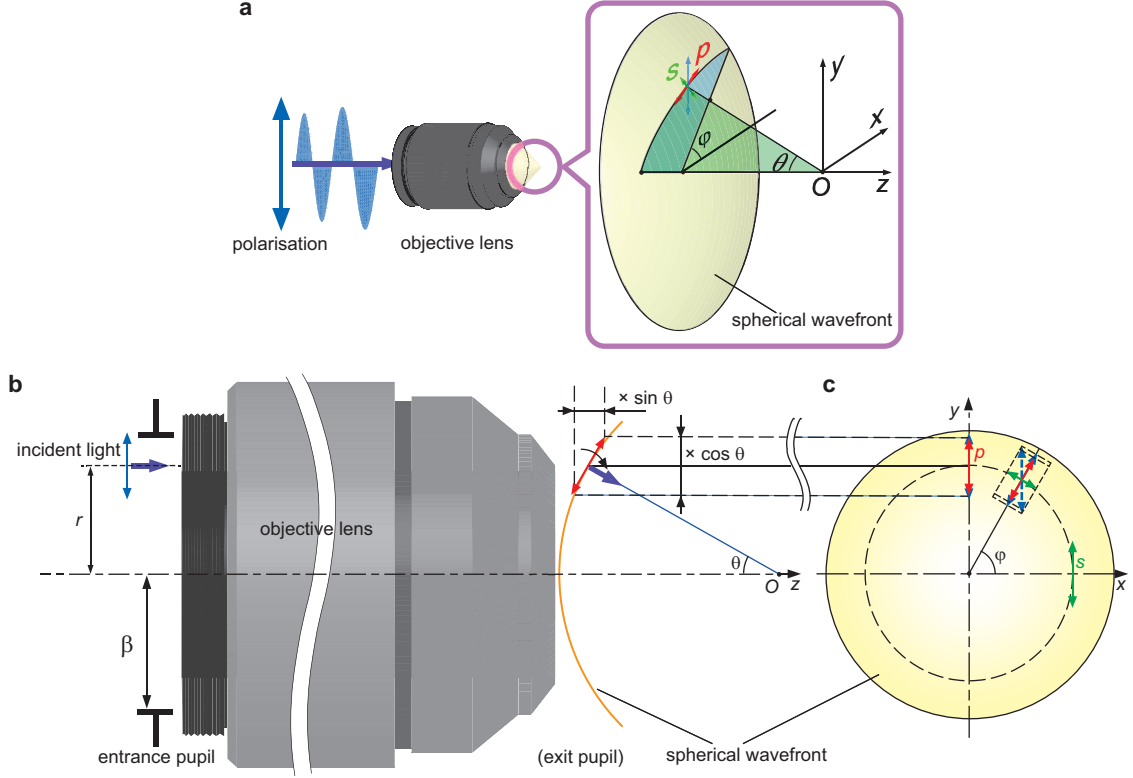


FIG. 4. **Vector nature of light amplitude in focusing.** **a**, Focusing of linearly polarised light through an objective lens. Vector amplitude of incident flat-wavefront light is mapped to that on spherical wavefront at the exit pupil of the objective lens. A position on the spherical wavefront is identified by the cone and directional angles, θ and φ , respectively. **b**, Cross-sectional view of **a** on a $z - \varphi$ plane. φ -directional component of the vector amplitude of incident light (blue arrows) is mapped to that (red arrows) on spherical wavefront by the objective lens. **c**, Front view of **a**. The objective lens tilts the p -component (radial component: red arrows) of a vector light amplitude but does nothing to the s -component (azimuthal component: green arrows). This causes inhomogeneous change in the light polarisation, because the decomposition into the p - and s -components depends on φ for linearly-polarised incident light.

expressed as a unit vector \hat{e}_{in} , where the components are a pair of complex numbers, α and β ($|\alpha|^2 + |\beta|^2 = 1$). Specifically, $\hat{e}_{\text{in}} = (\alpha, \beta) = \alpha \hat{x} + \beta \hat{y}$, where \hat{x} and \hat{y} represent unit vectors in the x and y directions, respectively. In particular, $(\alpha, \beta) = (1/\sqrt{2}, \mp i/\sqrt{2})$ describes the left

or right circular polarisation. When the incident light is expressed by the vector amplitude: $e^{-i\varphi} E_{\text{in}}(r) \hat{e}_{\text{in}}$ at the entrance pupil of the objective lens, electric field amplitude \mathbf{E} at the observation point (ρ, ϕ, z) in the image space is expressed as follows:

$$\begin{aligned} \mathbf{E}(\rho, \phi, z) = & \pi i^l k^2 \int_0^{\gamma_{\text{max}}} \sin \theta d\theta \mathcal{E}(\theta) \exp(ikz \cos \theta) e^{-i\ell\phi} \left\{ (1 + \cos \theta) J_l(k\rho \sin \theta) \hat{e}_{\text{in}} \right. \\ & - \sqrt{2}i \sin \theta [(\hat{e}_+, \hat{e}_{\text{in}}) J_{l+1}(k\rho \sin \theta) e^{-i\phi} - (\hat{e}_-, \hat{e}_{\text{in}}) J_{l-1}(k\rho \sin \theta) e^{i\phi}] \hat{e}_z \\ & \left. + (1 - \cos \theta) [(\hat{e}_+, \hat{e}_{\text{in}}) J_{l+2}(k\rho \sin \theta) e^{-2i\phi} \hat{e}_- + (\hat{e}_-, \hat{e}_{\text{in}}) J_{l-2}(k\rho \sin \theta) e^{2i\phi} \hat{e}_+] \right\}, \quad (7) \end{aligned}$$

where $\mathcal{E}(\theta)$ denotes the θ distribution of the incident-light amplitude [38] and γ_{max} denotes the maximum focusing angle [= $\sin^{-1}(\text{NA})$]. In Eq. (7), the inner product of the complex vectors is expressed as $\langle \mathbf{a}, \mathbf{b} \rangle (= \sum_i a_i^* b_i)$.

The relationship between $E_{\text{in}}(r)$ and $\mathcal{E}(\theta)$ is determined by the optical design of the objective lens. Generally, $E_{\text{in}}(\beta \sin \theta / \sin \gamma_{\text{max}}) = \mathcal{E}(\theta)$ holds. The objective lenses that satisfy the sine condition, where β denotes the

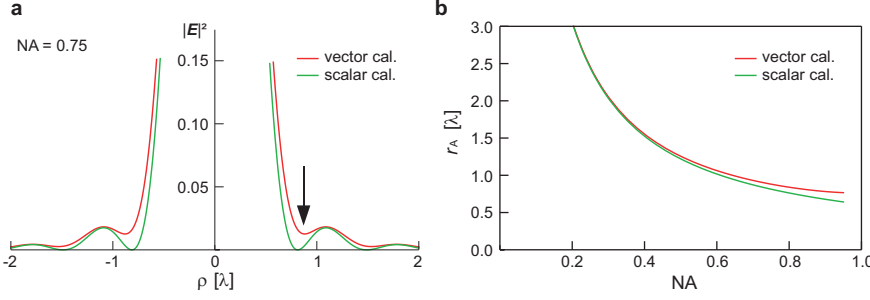


FIG. 5. **Comparison between scalar and vector calculations.** **a**, Cross-sectional profiles of focal patterns calculated by scalar diffraction formula (green line) and vector Debye integral (red line). Both of the profiles were calculated under the condition of $NA = 0.75$. **b**, Airy-disk radii as functions of NA. Results of scalar diffraction formula and vector Debye integral are plotted in green and red lines, respectively. The scale of length is selected as the wavelength of light in both **a** and **b**.

radius, for the entrance aperture). Based on Eq. (7), we can confirm that the circular-polarisation flat-wavefront ($l = 0$), the light presents a focal pattern identical to the mean of those of linear-polarisation (e.g., x - and y -polarisations) flat-wavefront light.

Airy-disk radius as function of NA. The super-resolution criterion proposed in the main text was established by selecting the radius of the Airy disk as a unit of length. The actual value of the Airy disk radius needs to be determined to assess whether an observed light spot array exceeds the super-resolution criterion under specific optical conditions. Thus, the proposed super-resolution criterion can be applied to varying focusing conditions by introducing the Airy disk radius and VP ratio, which are derived from calculations that appropriately reflect the focusing conditions.

An Airy disk was originally defined as the diffraction pattern of a circular aperture in the far-field region of light propagation and is derived from the scalar diffraction formula, which is proportional to $[J_1(k\rho NA)/(k\rho NA)]^2$ in image space. The distance from the centre of the image to the innermost dark ring is often referred to as the Airy disk radius, which is related to the conventional super-resolution criterion.

Equation (7) reproduces a focal pattern that is similar to that of a conventional Airy disk. However, a finite value was observed in the innermost dark ring (Fig. 5a). Therefore, the Airy disk radius is redefined as the distance from the optical axis to the innermost minimum in the high-NA regions. The redefined Airy disk radius is marginally larger than the conventional Airy disk radius, which is given by $0.61/NA$ in units of wavelength. The conventional and high-NA Airy disk radii are depicted as functions of NA in Fig. 5b to illustrate the difference between them. This difference is almost negligible for smaller NA values but becomes notable for $NA \gtrsim 0.7$.

Super-resolution criteria in high-NA regions.

Linear-polarisation flat-wavefront light produces a focal pattern as shown in Fig. 6a under high-NA focusing conditions. Consequently, the Airy disk radius has different values in the horizontal and vertical directions. Therefore, different length scales must be introduced to the horizontal and vertical spacings in a light spot array of

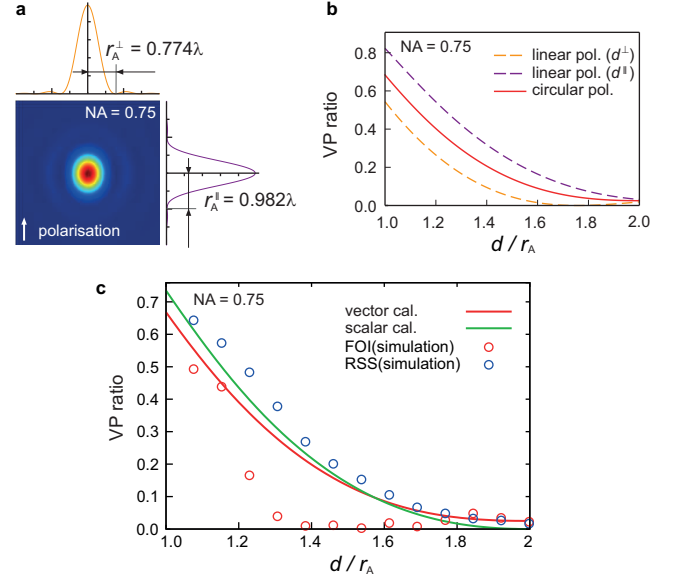


FIG. 6. **Effects of polarisation under condition of $NA = 0.75$.** **a**, Focal pattern and corresponding cross-sectional profiles of linear-polarisation light. **b**, Super-resolution criteria for circular-polarisation (solid red line) and y linear-polarisation (dashed lines) light. In case of linear-polarisation light, the super-resolution criteria act differently according to the light-polarisation direction (dashed purple line) and the perpendicular direction (dashed orange line). **c**, Comparison of numerical spot-array patterns with the super-resolution criteria. Open circles present spot spacing and VP ratio of the spot-array patterns obtained by applying the numerical hologram reproduction procedure (FFT) to holographic phase patterns designed by FOI (red open circles) and RSS (blue open circles) methods. Red and green solid curves display the super-resolution criteria calculated by the vector and scalar diffraction formulae, respectively.

linearly polarised light to derive the proposed criteria in the main text. Equation (7) indicates that a focal pattern with circular polarisation flat-wavefront light is determined by the horizontal and vertical components. This holds true, not strictly but effectively, up to the leading three digits of the Airy disk radius.

The super-resolution criteria calculated for linearly and circularly polarised light are presented in Figure 6b. Note that the Airy disk radius of the circularly polarised

light is used as the scale of length for all the results in Fig. 6b. The super-resolution criterion for circularly polarised light can be approximated as the mean of those for the horizontal and vertical linear-polarisation lights, as displayed in Fig. 6b. Thus, the super-resolution criterion for circularly polarised light is expected to be applicable to the evaluation of the mean spot spacing in a square light spot array of linearly polarised light.

To evaluate the super-resolution of a given light spot array, it is reasonable to adopt a super-resolution criterion calculated using an appropriate selection of the light propagation conditions under which the spot-array pattern was generated. As hologram optimisation is performed by applying the FFT, specifically through Fraunhofer diffraction calculation, the super-resolution

criterion for numerically generated light-spot patterns can be assessed using the scalar diffraction formula. Figure 6c suggests that the FOI-cost method can potentially produce super-resolution light spot arrays based on the super-resolution criterion (solid green line) calculated using the scalar diffraction formula.

However, the approximate condition of the scalar diffraction formula is not satisfied at a $NA = 0.75$, and the super-resolution cannot be determined from this numerical simulation. This provides insights into estimating the potential effectiveness of the method. As discussed in the main text, the VP ratio of the experimentally generated patterns exceeds the super-resolution criterion based on the vector Debye formula, indicating that super-resolution patterns were obtained using the FOI-cost method.